Received: 25 April 2022 | Revised: 20 April 2023 | Accepted: 8 May 2023

DOI: 10.33012/navi.599

ORIGINAL ARTICLE

A Case Study Analysis for Designing a Lunar Navigation Satellite System with Time Transfer from the Earth GPS

Sriramya Bhamidipati | **Tara Mina** | **Grace Gao**

Department of Aeronautics and Astronautics, Stanford University

Correspondence
Grace Gao
Department of Aeronautics and Astronautics, Stanford University
Stanford, CA, USA, 94305
Email: gracegao@stanford.edu

Abstract

There is growing interest in designing a future lunar navigation satellite system (LNSS) while utilizing a SmallSat platform. However, many design decisions, e.g., regarding the satellite clock and lunar orbit, are yet to be finalized. In our prior work, we developed an LNSS architecture that leverages intermittently available Earth-GPS signals to compute timing corrections, thereby alleviating the need for a higher-grade onboard clock. In this work, we formulate twenty case studies with different grades of clocks and lunar orbits to analyze the trade-offs in designing a SmallSat-based LNSS with time transfer from the Earth GPS. For each case study, the accuracy of ranging signals is assessed via the lunar user equivalent range error (UERE). Even with lower-grade clocks, the lunar UERE exhibits performance comparable to that of the Earth GPS. Furthermore, variations in the lunar UERE are also examined when the available Earth-GPS measurements are processed at different rates.

Keywords

case study analysis, lunar navigation satellite system, lunar uere, size weight and power (swap), smallsat, time transfer

1 | INTRODUCTION

Over a half century since the end of the Apollo program, the National Aeronautics and Space Administration (NASA) will return humans to the Moon. In the coming decade, through the Artemis missions, NASA will land the first woman and person of color on the lunar south pole (Smith et al., 2020). Additionally, many space agencies are participating in an international effort to establish a sustainable human presence on the Moon, which serves as a crucial platform to support future deep space exploration (Laurini & Gerstenmaier, 2014). Indeed, we are entering a second space race, with international space agencies planning over forty lunar missions in the next decade and with crucial involvement from commercial space industry companies, including SpaceX and Blue Origin. To support increasing plans for crewed and robotic activities, future lunar missions will require access to reliable and precise position, navigation, and timing (PNT) services everywhere on the Moon.

Recently, the NASA Goddard Space Flight Center and the European Space Agency (ESA) conceptualized global positioning system (GPS)-like satellite constellations around the Moon, named LunaNet (Israel et al., 2020) and Moonlight (Cozzens, 2021),

respectively. Furthermore, there has been an emerging interest in the use of a SmallSat platform for these PNT constellations to allow for cost-effectiveness and rapid deployment (Israel et al., 2020). According to Mabrouk, 2015, a SmallSat is about the size of a large kitchen fridge and weighs < 180 kg. These lunar PNT constellations by NASA and the ESA will assist in the overarching effort of establishing a sustainable human presence on the Moon by providing global PNT and communication services to lunar users. In particular, in the next decade, these initiatives will seek to satisfy needs expressed by the global exploration community, with a targeted position accuracy of less than 50 m for lunar users (InsideGNSS, 2021).

While the lunar positioning accuracy of a lunar navigation satellite system (LNSS) depends on a variety of different factors, a few key factors are as follows: a) the lunar user equivalent ranging error (UERE), which determines the ranging accuracy of transmitted satellite signals, b) the minimum received power, which affects the signal acquisition and tracking performance, c) the constellation size, which ensures the visibility of a minimum number of LNSS satellites for any lunar user at any time, d) the geometric dilution of precision, which evaluates the effect of measurement error on the estimated position covariance, and e) the overall cost, which depends on the costs of launches from Earth, the costs of injection into a stable orbit around the Moon, and onboard equipment and maintenance costs. To provide a systematic approach, the current work assesses the LNSS design in terms of lunar UERE, while assessments for other factors will be explored in future works.

Given that the lunar PNT constellation initiatives are in the preliminary design phases, the LNSS design involves finalizing many key design considerations, including the following:

- Lunar satellite orbit. Several types of lunar orbits that have previously been investigated include low lunar orbits (LLOs), prograde circular orbits (PCOs), near-rectilinear halo orbits (NRHOs), and elliptical lunar frozen orbits (ELFOs). In particular, ELFOs refer to a specific category of *frozen orbits* providing a greater coverage of the lunar poles, wherein *frozen* orbits represent those orbits that maintain nearly constant orbital parameters for extensive periods of time, without requiring station-keeping (Folta & Quinn, 2006; Whitley & Martinez, 2016). Although PCOs are not frozen, they maintain multi-year stability with orbital parameters exhibiting predictable, repeatable behavior (Whitley & Martinez, 2016). Due to the low orbiting altitude, LLOs have shorter orbital periods around the Moon, and there exist a few inclinations at which LLOs are also considered to be frozen or quasi-frozen (Folta & Quinn, 2006). While NRHOs are less stable than the above orbits, thereby requiring more frequent station-keeping maneuvers, these orbits are highly elliptical, with nearly constant visibility of Earth and the lunar poles (Schonfeldt et al., 2020).
- Onboard satellite clock. The choice of onboard clock is critical for designing a navigation system, as its grade (which depends on timing stability) directly affects the ranging precision offered to lunar users. Among various clock choices is the commercial chip-scale atomic clock (CSAC) with its radiation tolerance and low size, weight, and power (SWaP), which has been specifically developed for space applications (Schmittberger & Scherer, 2020). Another potential clock choice is the deep space atomic clock (DSAC), which has been recently designed by NASA to provide greater long-term timing stability and to assist in spacecraft radio navigation (T. Ely et al., 2022; T. A. Ely et al., 2018; Seubert et al., 2022).

Furthermore, designing a SmallSat-based LNSS involves unique challenges as compared with the legacy Earth GPS, which lead to the following additional design limitations: a) Limited size of LNSS satellites. A SmallSat platform limits its payload capacity, including the SWaP of the onboard clock. Given that lower-SWaP clocks tend to have worse timing stabilities (Schmittberger & Scherer, 2020), the SWaP limitation on the clock directly affects the timing stability. b) Limited ability to monitor LNSS satellites. Given that a limited number of ground monitoring stations can be established on the Moon and that resources on Earth for monitoring the lunar constellation are limited, it is desirable for the LNSS satellites to require less maintenance, including fewer station-keeping maneuvers and clock correction updates. c) Increased orbital perturbations in the lunar environment. Because the Moon has a highly nonuniform distribution of mass (Melosh et al., 2013), its gravitation field is more anisotropic than that of Earth. In addition, Earth's gravity can significantly impact satellites in high-altitude orbits around the Moon, thereby limiting the set of feasible and stable lunar orbits.

Given these challenges for designing a PNT constellation in the lunar environment, one may consider the potential of leveraging the existing Earth's legacy GPS, which is equipped with higher-grade atomic clocks and an extensive ground monitoring network. At lunar distances of approximately 385000 km, the Earth-GPS signal is significantly attenuated, and the Earth-GPS satellites directed toward Earth are largely occluded by Earth and often the Moon. This limits the Earth-GPS signal availability at lunar distances, with signals coming only the Earth-GPS transmitting antenna's side lobes and the small, unoccluded parts of the main lobe. NASA's Magnetospheric Multiscale Mission (MMS) has used these largely attenuated and intermittently available Earth-GPS signals to successfully compute position estimates in space (L. B. Winternitz et al., 2017). In fact, the MMS broke the Guinness World Record for the highest altitude for achieving an Earth-GPS fix in 2016 at distances of approximately one-fifth of the distance to the Moon (Johnson-Groh, 2016; L. B. Winternitz et al., 2017) and then surpassed its previous record in 2019 by obtaining a fix at approximately half of the distance to the Moon (Baird, 2019). Several simulation works have also demonstrated the feasibility of using the Earth GPS at lunar distances (Cheung et al., 2020; Schonfeldt et al., 2020; L. B. Winternitz et al., 2019). Through its GPS Antenna Characterization Experiment (ACE) study, NASA has characterized GPS antenna gain patterns at high elevation angles from boresight for space users (Donaldson et al., 2020). NASA has also developed a spaceborne Earth-GPS receiver (L. Winternitz et al., 2004), which will be tested on the lunar surface for the first time in 2023, as a part of the Lunar GNSS Receiver Experiment (LuGRE) (InsideGNSS, 2021; Kraft, 2020). Additionally, in 2023, the ESA will launch the Lunar Pathfinder communication satellite to the Moon, which will utilize a spaceborne, high-sensitivity Earth-GPS receiver to provide a position fix for the first time in lunar orbit (Cozzens, 2021).

In our prior work (Bhamidipati et al., 2021, 2022a), we designed an LNSS architecture that harnessed the legacy Earth GPS to provide precise timing corrections to the onboard clock, as depicted in Figure 1. The time-transfer technique leverages intermittently available Earth-GPS signals to alleviate the SWaP requirements of the onboard clocks and to mitigate the need for an extensive ground monitoring infrastructure on the Moon. We also devised a mathematical formulation of a lunar UERE metric, which is proportional to the root mean square (RMS) timing error, to analyze the ranging accuracy of an LNSS satellite. This proposed method achieved a low lunar UERE of less than 10 m while using a low-SWaP CSAC for an LNSS satellite in an ELFO.

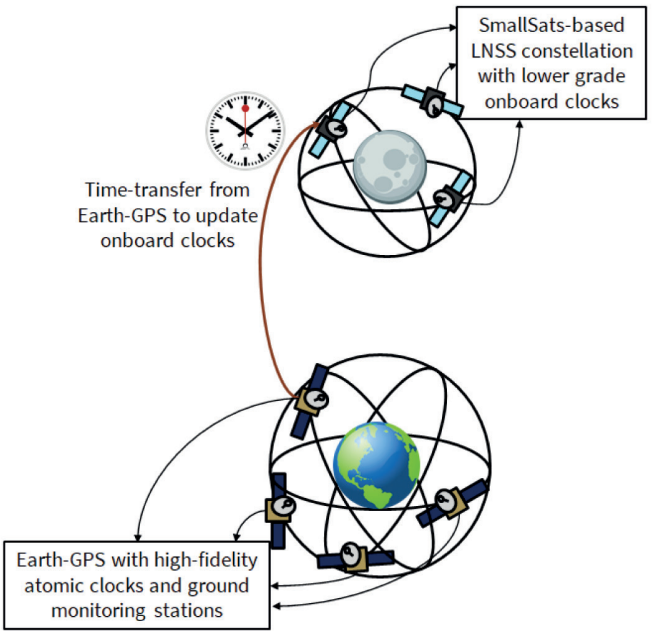

FIGURE 1 Architecture of the proposed time transfer from the Earth GPS (Bhamidipati et al., 2021), which utilizes intermittently available Earth-GPS signals to correct the lower-grade clocks onboard the LNSS satellite

Given that many design choices, including the grade of the onboard clock and the orbit type, still need to be finalized for the future SmallSat-based LNSS, in this study, we extend upon prior work (Bhamidipati et al., 2021, 2022a) to analyze the LNSS performance using the proposed time-transfer architecture (in Figure 1) from the Earth GPS under various case studies. Specifically, an LNSS satellite is simulated in various lunar orbit types, including an ELFO, LLO, PCO, and NRHO, and equipped with different grades of onboard clocks. For a given LNSS satellite orbit, the Earth-GPS continual outage period (ECOP) metric is examined to analyze the visibility effects of the Earth GPS on the performance of onboard clock corrections. The lunar UERE metric is estimated to perform a comparison across different case studies. Through this analysis, a trade-off can be observed between the different design considerations of the onboard clock and orbit type for an LNSS design that leverages the Earth-GPS time transfer. Furthermore, a variation in the lunar UERE is observed for different rates of collecting available Earth-GPS measurements (see Section 4.4 for the results of this sensitivity analysis). This analysis provides insights into the extent of Earth-GPS signal tracking and processing required to provide sufficient ranging precision. In particular, less frequent use of Earth-GPS measurements would allow the LNSS satellite to continually switch off the onboard Earth-GPS receiver for longer periods of time in order to save power. Across the various case studies, the time-transfer architecture allows the LNSS to achieve a performance comparable to that of the legacy Earth GPS, even while using a low-SWaP onboard clock. This work is based on our recent 2022 Institute of Navigation International Technical Meeting conference paper (Bhamidipati, Mina, & Gao, 2022b).

1.1 | Key Contributions

The key contributions of this paper are as follows:

1. We design various case studies related to the grade of onboard clocks and orbit types for analyzing the trade-offs in designing an LNSS with time

transfer from the Earth GPS. In particular, five clock types are investigated, with diverse SWaP characteristics that range from a low-SWaP CSAC to a high-SWaP DSAC (T. A. Ely et al., 2018) developed by NASA. Additionally, four previously studied lunar orbit types are investigated, namely, the ELFO, NRHO, LLO, and PCO.

2. A comparison analysis is performed across various case studies by investigating the associated RMS timing errors. Note that the RMS timing errors are primarily governed by the duration for which no Earth-GPS satellites are visible (ECOP metric) and the geometric configuration between the Earth-GPS constellation and the LNSS satellite (occultations due to Earth and the Moon).
3. The lunar UERE metric is evaluated for each case study and demonstrates a measurement ranging accuracy comparable to that of the legacy Earth GPS, even for a low-SWaP onboard clock.
4. Additionally, the variation in the lunar UERE is examined for different rates of collecting Earth-GPS measurements. This analysis provides insight into the extent of Earth-GPS signal processing required and, correspondingly, the amount of power required to operate the onboard Earth-GPS receiver, in order to provide sufficient ranging precision.

The remainder of this paper is organized as follows. Section 2 summarizes the previously proposed time-transfer architecture from the Earth GPS to the LNSS (Bhamidipati et al., 2021) and describes the modifications incorporated to conduct further analysis. Section 3 provides a high-level overview of various case studies and describes the high-fidelity lunar simulation setup used, which involves modeling the onboard clock and orbit for each case study. Section 4 discusses the implications of our case study analysis in designing an LNSS. Section 5 provides concluding remarks.

2 | TIME TRANSFER FROM THE EARTH GPS TO THE LNSS

This section summarizes our prior work (Bhamidipati et al., 2021) on time transfer from the Earth GPS, wherein an LNSS satellite is considered to be equipped with an Earth-GPS receiver and an onboard clock that can provide short-term timing stability. A timing Kalman filter (Krawinkel & Schön, 2015; Zucca & Tavella, 2005) updates the LNSS satellite clock with the intermittently available Earth-GPS signals and formulates the lunar UERE metric to characterize the ranging accuracy of transmitted navigation signals. An overview is also provided on the aspects of further analysis conducted in this work. In particular, the sensitivity of the lunar UERE metric in different simulated case studies is analyzed, including modifications of the measurement update rate for the proposed timing Kalman filter.

For any LNSS satellite, the proposed filter maintains the LNSS clock estimate at each time epoch t by propagating the following timing state vector: $x_t := [b_t \quad \dot{b}_t]^\top$, where b_t is the clock bias state in m and $\dot{b}_t$ is the clock drift in ms^{-1}, with units converted from the timing domain through multiplication by the speed of light $c = 299792458$ m/s.

To maintain the LNSS clock estimate, the timing Kalman filter performs a *time update* every T_{pred} seconds, based on the clock error propagation model. For this, the associated process noise covariance Q is defined in terms of the power spectral density (PSD) coefficients h_0, h_{-1}, h_{-2} from an Allan deviation plot for the clock (Krawinkel & Schön, 2015). These PSD coefficients reflect the short-term and long-term stability of the onboard clock and can be heuristically computed

from the Allan deviation plots of a clock based on equations derived in (Van Dierendonck & McGraw, 1984). To perform time transfer from the Earth GPS, the filter first determines whether any Earth-GPS signals are visible by examining the received carrier-to-noise density ratio C/N_0. Then, the timing Kalman filter conducts a *measurement update* for the available Earth-GPS measurements with sufficiently high C/N_0.

During the measurement update step, the expected pseudorange and pseudorange rates are determined from the visible Earth-GPS satellites to form a measurement vector of residuals. In particular, the measurement residual vector is formulated by leveraging the LNSS satellite position and velocity information from the available ephemeris. Indeed, the LNSS satellites are expected to maintain real-time position and velocity estimations within a target accuracy, although the exact framework and assisting infrastructure (e.g., ground monitoring, lunar base stations, etc.) for doing so have not yet been finalized (National Aeronautics and Space Administration, 2022). Relativistic effects between the Earth-GPS satellite transmitter and lunar satellite receiver are not simulated in this work, but are left for future work. However, with a relativistic correction model, the LNSS satellite can correspondingly apply this correction to the received Earth-GPS measurements to formulate the measurement residual vector.

The measurement covariance matrix is modeled as a time-dependent diagonal matrix (Bhamidipati et al., 2021), based on the tracking errors of the receiver delay lock loop (Capuano, Basile, et al., 2015; Capuano, Botteron, et al., 2015; Kaplan & Hegarty, 2017) and phase lock loop (Borio et al., 2011; Capuano, Basile, et al., 2015) as well as the Earth-GPS UERE (Kaplan & Hegarty, 2017) and the expected error in the available LNSS satellite ephemeris. With the measurement vector and modeled measurement covariance, the filter applies corrections to the predicted timing state via standard Kalman filter expressions to obtain the updated state $\hat{x}_t$ and covariance.

Based on the RMS error in the filter estimate, we formulate a lunar UERE metric that characterizes the accuracy of the LNSS ranging signals for lunar users. On the Moon, any atmospheric delays are minimal. Moreover, multipath effects experienced by users on the lunar surface are considered to be negligible due to the lack of building infrastructure and foliage. As a result, the final lunar UERE can be computed in terms of the four most significant error components as follows:

$$\sigma_{\text{UERE, LNSS}} = \sqrt{\sigma^2_{\text{clk, LNSS}} + \sigma^2_{\text{gd, LNSS}} + \sigma^2_{\text{eph, LNSS}} + \sigma^2_{\text{rec, LNSS}}} \tag{1}$$

where the errors due to the differential group delay $\sigma_{\text{gd, LNSS}}$ and receiver noise $\sigma_{\text{rec, LNSS}}$ will depend on the final LNSS signal structure and lunar user receiver. Note that because the timing filter uses the LNSS satellite position and velocity information from the ephemeris, the lunar ephemeris error component $\sigma_{\text{eph, LNSS}}$ directly impacts the pseudorange residual measurement received at the LNSS, which will thus also affect the LNSS clock error $\sigma_{\text{clk, LNSS}}$.

In this work, the variation in the LNSS clock error component $\sigma_{\text{clk, LNSS}}$ is investigated for various grades of onboard clocks and various types of lunar orbits, and the corresponding impact on the overall lunar UERE is analyzed. Additionally, the impact on the lunar UERE is investigated for a potentially reduced measurement update rate when Earth-GPS signals are available, with a sampling period of $T_{\text{meas}} = mT_{\text{pred}}$, where m is a positive integer. Indeed, a larger choice of m corresponds to less frequent GPS measurement updates, which allows the spaceborne Earth-GPS receiver onboard an LNSS satellite to be switched off for longer durations of time to save power.

3 | OVERVIEW OF CASE STUDIES ON CLOCKS AND ORBITS

An extensive case study analysis is performed to examine the trade-off between different choices of onboard clocks and orbit types that can be considered for designing an LNSS with time transfer from the Earth GPS. In particular, a high-fidelity simulation is developed for an LNSS satellite for each orbit type using the Systems Tool Kit (STK) software by Analytical Graphics, Inc. (AGI, 2021). For each modeled orbit type, case studies are developed in MATLAB by simulating various grades of onboard clocks. For each case study, the start time epoch is 9 Nov 2025 00 : 00 : 00.000 UTC, and the experiment time duration is 2 months (equal to 61 days).

First, an overview is provided of the case studies related to the onboard clocks and lunar orbit types investigated in this work. Thereafter, the simulation steps are presented, as executed in the STK software and MATLAB for modeling the transmission and reception of Earth-GPS signals in each case study, which are based on the previous validation framework (Bhamidipati et al., 2021).

As mentioned in Section 1, many prior studies (Delépaut et al., 2020; Schönfeldt et al., 2020) have investigated various types of lunar orbits, primarily based on their stability and the duration for which their stability can be ensured. The lunar orbit types for this work include the ELFO, NRHO, LLO, and PCO, whose coverage and stability characteristics are discussed in Section 1. Realistic simulations are created for an LNSS satellite in different lunar orbits by leveraging the high-precision orbit propagator (HPOP) in the STK software (AGI, 2021). The HPOP generates and propagates accurate position and velocity solutions of the LNSS satellite by accounting for precise force models of the Earth, Sun, and Moon. Note that, in this paper, all of the orbits are naturally propagated using the HPOP, and no station-keeping is involved.

Three orbit types are modeled, namely, the ELFO, LLO and PCO, in the STK software using classical orbit mechanics (Montenbruck et al., 2002). With this approach, objects orbiting in space require six elements (six Keplerian parameters) to fully characterize their position and velocity at any point in time. Specifically, prior literature (Delépaut et al., 2020; T. A. Ely & Lieb, 2006; Whitley & Martinez, 2016) on ELFOs, LLOs, and PCOs defines their corresponding six Keplerian parameters at the start time epoch, including the semi-major axis, eccentricity, inclination, argument of perigee, right ascension of the ascending node (RAAN), and mean anomaly. Table 1 lists the associated Keplerian parameters of the three lunar orbit types, while Figure 2 shows associated illustrations in the Moon's inertial frame.

In contrast, to model the fourth lunar orbit type in this case study analysis, namely, the L2 south NRHO, the initial position $[r_x, r_y, r_z]$, and velocity $[v_x, v_y, v_z]$ are specified in the Moon-centered Earth–Moon rotating frame. Defining the

TABLE 1
Keplerian Parameters for Three (ELFO, LLO, and PCO) of the Four Lunar Orbit Types Considered in This Case Study Analysis

Orbit Type	Orbital Period (hr)	Semi-major Axis (km)	Eccentricity	Inclination (°)	Argument of Perigee (°)	RAAN (°)	Mean Anomaly (°)
ELFO	24	9750.5	0.7	63.5	90	0	0
LLO	2	1837.4	0.0	28.5	0	0	0
PCO	8.1	4737.4	0.0	75.0	0	90	0

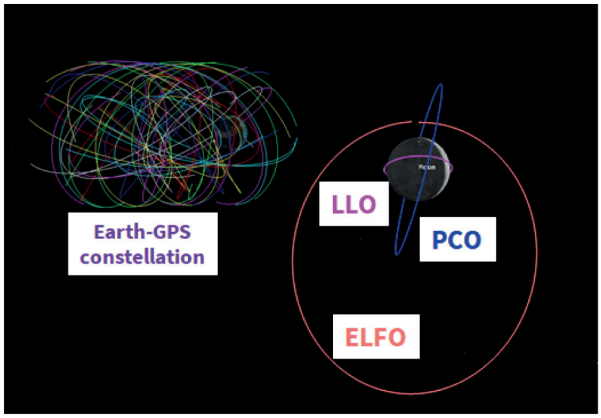

FIGURE 2 Illustration of three (ELFO, LLO, and PCO) of the four lunar orbit types considered in this case study analysis
All of these orbits are visualized in the Moon's inertial frame. The semi-major axis is 9750.5 km for the ELFO (orange), 1837.4 km for the LLO (magenta), and 4737.4 km for the PCO (blue). The HPOP tool in STK is used to propagate the initial conditions defined by the Keplerian parameters of these orbits in Table 1.

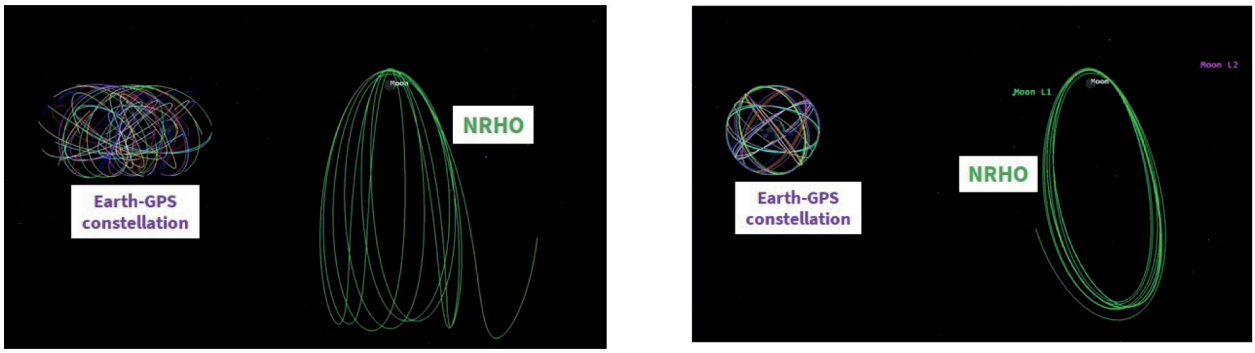

(a) (b)

FIGURE 3 The NRHO (L2, radius of perigee = 4500 km, south family) visualized in (a) the Moon's inertial frame and (b) the Moon-centered Earth–Moon rotating frame
The x-axis of the Earth–Moon rotating frame is along the instantaneous Earth–Moon position vector, the z-axis is along the instantaneous angular momentum vector of the Moon's orbit around the Earth, and the y-axis completes the orthogonal system. The HPOP tool in STK is used to propagate the NRHO orbit from its initial state vector defined in (Williams et al., 2017).

initial conditions in an Earth–Moon rotating frame is particularly useful when discussing halo orbits in the Earth–Moon system (Williams et al., 2017). In the Earth–Moon rotating frame, the x-axis is along the instantaneous Earth–Moon position vector, the z-axis is along the instantaneous angular momentum vector of the Moon's orbit around the Earth, and the y-axis completes the orthogonal system. Specifically, this approach is based on prior literature (Williams et al., 2017) that solves for an NRHO in the ephemeris model (L2, radius of perigee of 4500 km, south family) using a forward/backward shooting process to provide the following initial state vector at an initial time epoch of 8 Nov 2025 23 : 22 : 07.10353 TDB: $r_x = -125.952$ km, $r_y = 120.961$ km, $r_z = 4357.681$ km, $v_x = -0.042$ km/s, $v_y = 1.468$ km/s, and $v_z = -0.003$ km/s. The orbital period for this NRHO orbit is approximately 171.5 hr. Illustrations of the designed NRHO in both the Moon's inertial frame (similar to that in Figure 2) and the Moon-centered Earth–Moon rotating frame are shown in Figures 3(a) and 3(b), respectively.

TABLE 2
SWaP Characteristics, Time Deviation, and PSD Coefficients of the Five Clock Types Considered in This Case Study Analysis
SWaP and TDEV values were taken from (Schmittberger & Scherer, 2020) while PSD coefficients were computed from their respective Allan deviation plots. The Allan deviation plot for CSAC was taken from Lutwak, 2011. For the higher-grade RAFS clock and DSAC, the Allan deviation plots found in the literature (Almat, 2020; T. A. Ely et al., 2018) do not capture the effects of noise components related to the h_{-1} and h_{-2} coefficients. As a result, after a confirmation based on heuristic analysis, the process noise covariance Q terms depending on h_{-1} and h_{-2} are considered to be negligible for the RAFS and DSAC.

Clock type	Size (cm^3)	Weight (kg)	Power (W)	TDEV per day (μs)	PSD coefficients		
					h_0	h_{-1}	h_{-2}
Microchip CSAC	17	0.035	0.1	1.5×10^{-6}	1.3×10^{-20}	1.0×10^{-24}	3.7×10^{-29}
Microchip MAC	50	0.084	5	1.7×10^{-7}	4.7×10^{-22}	1.2×10^{-25}	1.7×10^{-30}
SRS PRS10	155	0.6	14.4	7.0×10^{-8}	1.3×10^{-22}	2.3×10^{-26}	3.3×10^{-31}
Excelitas RAFS	1645	6.35	39	4.8×10^{-9}	8.0×10^{-24}	-	-
NASA DSAC	17000	16	47	4.0×10^{-11}	1.8×10^{-25}	-	-

Given the interest in the SmallSat platform for the future LNSS, various case studies of onboard clock types are chosen while keeping in mind that the limited payload capacity restricts the SWaP of the onboard clock. Based on prior literature (Schmittberger & Scherer, 2020), the clock types for this work include Microchip's CSAC, Microchip's micro atomic clock (MAC), the Stanford Research Systems (SRS) PRS10, Excelitas' rubidium atomic frequency standard (RAFS), and NASA's DSAC (T. A. Ely et al., 2018). The specifications of these clock types are listed in Table 2, which have been arranged in increasing order of their SWaP for convenience. Note that the Microchip MAC and SRS PRS10 are not space-qualified clocks and have been considered in this case study analysis as a way to incorporate options for increasing the magnitude of timing stabilities from low-cost CSAC to high-SWaP DSAC. Moreover, DSAC is included in order to provide a benchmark in terms of the current state-of-the-art timing stability that can be attained in deep space. For each clock type, the true clock error model is simulated in MATLAB to have a constant drift in the clock bias, and thereafter, the clock states are propagated forward in time using a first-order state transition matrix. The true clock drift (constant value) is assigned based on the known specifications of time deviation (TDEV) observed at the end of a day, which are reported in Table 2. Note that for any clock type, TDEV refers to the expected error in reported time after a certain holdover time, which essentially depends on the Allan deviation and frequency drift. For the *time update* in the timing filter described in Section 2, the PSD coefficients listed in Table 2 are used to model the corresponding process noise covariance matrix Q.

For the chosen LNSS satellite clock and orbit type in each case study, the simulation scenario is modeled in the STK software and MATLAB to compute C/N_0 and the measurement residual vector for visible Earth-GPS satellites, which are later given as input to our timing filter. The key modeling aspects are summarized below, while a more detailed explanation has been provided in our earlier work (Bhamidipati et al., 2021).

First, the simulated Earth-GPS constellation consists of 31 satellites with 8 satellites from Block IIR, 7 from IIRM, 12 from IIF, and 4 from Block III. While the performance for a standalone Earth-GPS L1 C/A lunar receiver is examined in this work, this proposed time-transfer architecture can be applied to other terrestrial signals from other global navigation satellite system (GNSS) constellations, such as the GPS L5 and the Galileo E1 and E5 signals, which have also been considered

in prior works (Capuano, Basile, et al., 2015; Capuano, Botteron, et al., 2015). The additional terrestrial GNSS signals are expected to result in better lunar UERE values with the proposed time-transfer architecture, due to the corresponding increase in received measurements. The transmission antennas on Earth-GPS satellites are modeled by utilizing the transmission power and antenna gain patterns of the L1 C/A signals, which are available from the NASA GPS ACE study (Donaldson et al., 2020). Next, a spaceborne Earth-GPS receiver is simulated with a steering antenna pointed toward the Earth so as to maximize the visibility of Earth-GPS signals at the LNSS satellite. Based on prior literature (Capuano, Basile, et al., 2015; Delépaut et al., 2019), a high-gain antenna is considered with 14 dBi at an off-boresight angle of 0° and a 3-dB beamwidth of 12.2°. For details regarding the approximate sizing of the high-gain antennas and their gimbals/steering equipment, the reader is directed to the LuGRE mission, the details of which can be found in Table 2 of Parker et al., 2022. Based on the specifications detailed in Parker et al., 2022 and past missions (Wertz et al., 2011), the mass of an LNSS satellite is heuristically computed to be 133.3 kg in Bhamidipati, Mina, Sanchez, et al., 2022. This finding ensures that the mass of the LNSS case studies discussed in this paper conforms to the SmallSat constraint, which was reported in Section 1 as < 180 kg. For more details, refer to Section 3.2 of Bhamidipati, Mina, Sanchez, et al., 2022. An Earth-GPS satellite is considered to be visible when, for a continuous time duration of at least 40 s, the received C/N_0 value is greater than 15 dB-Hz, which is a conservative threshold for acquisition and tracking determined from prior works (Capuano, Basile, et al., 2015; Capuano, Botteron, et al., 2015; Delépaut et al., 2020).

Finally, measurements received at the LNSS satellite are simulated by incorporating the true clock bias and drift in the true range and range rate between the visible Earth-GPS and LNSS satellites, respectively. Note that the C/N_0, true range, and range rate values are extracted from the STK simulation, whereas the true clock bias and drift are obtained from the simulated clock error model in MATLAB. To formulate the residual vector given to the *measurement update* explained in Section 2, stochastic errors are induced based on simulated uncertainties from the receiver tracking loops.

4 | CASE STUDY ANALYSIS: RESULTS AND DISCUSSION

For designing an LNSS with time transfer from the Earth GPS, the trade-off across different case studies is analyzed with respect to the onboard clock and orbit type, as listed in Section 3.

To characterize the lunar UERE discussed in Section 2, the group delay and receiver noise error magnitudes are taken to be the same as those of the Earth GPS, i.e., $\sigma_{\text{gd, LNSS}} = 0.15$ m and $\sigma_{\text{rec, LNSS}} = 0.1$ m. Given that the future LNSS will have greater limitations on ground monitoring infrastructure than the Earth GPS, the error component due to the broadcast ephemeris is scaled in the lunar UERE as $\sigma_{\text{eph, LNSS}} = 3$ m. This value is essentially one order of magnitude higher than that of the Earth GPS and aligns with the desired position requirements of lunar navigation satellites listed in National Aeronautics and Space Administration, 2022, i.e., < 4 m, 1-σ RSS. Our prior work provides a sensitivity analysis (Bhamidipati, Mina, & Gao, 2022a), wherein the timing errors and lunar UERE values are analyzed as the ephemeris errors vary at 0.3 m, 3 m, 30 m, and 300 m. The timing filter's *time update* step is executed every $T_{\text{pred}} = 60$ s. Details regarding the reduced update rate with a sampling period of $T_{\text{meas}} = mT_{\text{pred}}$ for the *measurement update* will be discussed below.

4.1 | Validation Metrics

To perform a comparison analysis across different case studies, the following four validation metrics are defined:

1. Satellite visibility, which indicates the percentage time of the entire experiment duration for which the number of visible Earth-GPS satellites is greater than a pre-specified threshold. Two satellite visibility parameters are examined: a) the percentage time for which at least 1 Earth-GPS satellite is visible, as this is the minimum number required to estimate the clock bias and drift; b) the percentage time for which at least 4 Earth-GPS satellites are visible, as this is the minimum number required to estimate the full state vector, which includes the position, clock bias, velocity, and clock drift.
2. Maximum ECOP to identify the region of maximum continuous time when no Earth-GPS satellites are visible.
3. RMS errors in clock estimates across the entire simulation time duration to analyze the performance of the Earth-GPS time transfer for a reduced measurement update rate with a sampling period of $T_{\text{meas}} = mT_{\text{pred}}$ and $m = 5$.
4. Lunar UERE metric, which characterizes the ranging measurement accuracy of signals transmitted by an LNSS satellite. As explained in Section 2, the lunar UERE metric depends on the RMS error in the clock bias.

A case study is considered to be desirable if it exhibits either some or all of the following: greatest satellite visibility, shortest maximum ECOP, and lowest lunar UERE. To perform a sensitivity analysis of the examined case studies, the lunar UERE metric is computed for different reduced measurement update rates with $m = 1, 5, 30, 60$. Note that $m = 1$ provides a baseline comparison (non-reduced rate), as it depicts the case in which the measurement update step is executed whenever Earth-GPS satellites are visible, corresponding to the original framework of the timing filter proposed in our prior work (Bhamidipati et al., 2021).

4.2 | Across Orbit Types: Variation in Satellite Visibility and Maximum ECOP

For the four orbit types considered in this case study, the number of visible Earth-GPS satellites is shown in blue in Figures 4(a)–4(h) while the highlighted red vertical bars indicate the regions of ECOP. Based on Table 3, the NRHO achieves the highest visibility for at least one satellite, which is 99.9% of the total time, and the highest visibility for at least four satellites, which is 92.9% of the total time. The NRHO also exhibits the shortest maximum ECOP of only 420 s, while the other orbit types experience an ECOP of at least 2880 s. These observations related to the NRHO seem reasonable, as an LNSS satellite in the NRHO operates at high altitudes of 4500−700000 km above the Moon's surface and thus experiences fewer occultations from Earth and the Moon. By comparing the magnified plots in Figures 4(b), 4(d), 4(f), and 4(h), one can observe that the LLO, which has a low altitude of 100 km, exhibits the smallest time spacing between consecutive regions of ECOP. Furthermore, note that these magnified plots capture ECOPs experienced by different orbit types over a random two-day period and do not necessarily showcase the maximum ECOP occurrences.

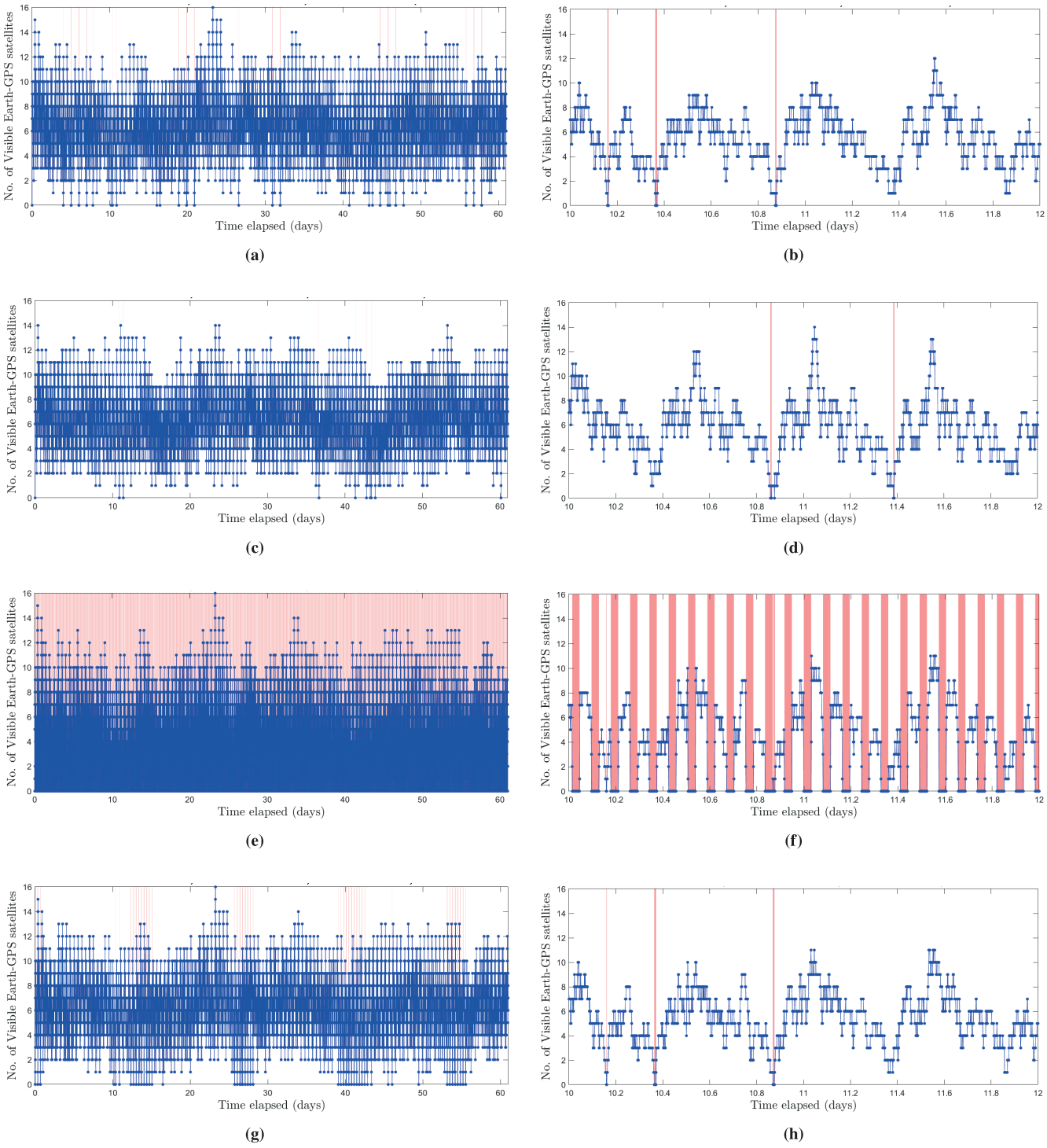

FIGURE 4 Earth-GPS satellite visibility and maximum ECOP across different orbit types The blue dotted lines indicate the number of visible Earth-GPS satellites, and the red vertical bars indicate regions of ECOP. (a), (c), (e), and (g) show the satellite visibility for the entire time duration for the ELFO, NRHO, LLO, and PCO, respectively. (b), (d), (f), and (h) show the magnified satellite visibility for a shorter time segment of 2 days. The NRHO not only exhibits the shortest maximum ECOP of 420 s but also the greatest visibility for at least one satellite at 99.9%.

4.3 | Across Clock Types: Variation in RMS Timing Errors

Table 4 compares the RMS estimation error in clock bias and drift across different case studies. Intuitively, the RMS timing error provides insights regarding

TABLE 3
Comparison Analysis Across Different Orbit Types

Orbit Type	Max ECOP (s)	Satellite Visibility (%)	
		≥ 1	≥ 4
ELFO	3360	99.2	92.1
NRHO	**420**	**99.9**	**92.9**
LLO	2880	61.5	55.6
PCO	3900	98.1	90.8

Note: Across the different orbit types, we observe that NRHO exhibits the shortest Maximum ECOP and Highest Visibility for at Least One and at Least Four Earth-GPS Satellites

TABLE 4
Comparison Analysis Across Different Onboard Clock and Orbit Types
As the clock SWaP increases (indicating a higher-grade clock), the timing stability is correspondingly less sensitive to the choice of orbit type.

RMS Timing Error in Clock Type		ELFO	NRHO	LLO	PCO
Microchip CSAC	**Bias** (μs)	4.05×10^{-2}	3.83×10^{-2}	6.79×10^{-2}	4.08×10^{-2}
	Drift (ns/s)	4.07×10^{-2}	4.01×10^{-2}	4.19×10^{-2}	4.04×10^{-2}
Microchip MAC	**Bias** (μs)	2.13×10^{-2}	2.15×10^{-2}	2.78×10^{-2}	2.17×10^{-2}
	Drift (ns/s)	0.81×10^{-2}	0.81×10^{-2}	0.81×10^{-2}	0.83×10^{-2}
SRS PRS10	**Bias** (μs)	1.76×10^{-2}	1.77×10^{-2}	2.13×10^{-2}	1.78×10^{-2}
	Drift (ns/s)	0.45×10^{-2}	0.46×10^{-2}	0.45×10^{-2}	0.46×10^{-2}
Excelitas RAFS	**Bias** (μs)	1.23×10^{-2}	1.21×10^{-2}	1.43×10^{-2}	1.21×10^{-2}
	Drift (ns/s)	0.15×10^{-2}	0.15×10^{-2}	0.15×10^{-2}	0.15×10^{-2}
NASA's DSAC	**Bias** (μs)	$\mathbf{0.79} \times 10^{-2}$	$\mathbf{0.76} \times 10^{-2}$	$\mathbf{0.87} \times 10^{-2}$	$\mathbf{0.74} \times 10^{-2}$
	Drift (ns/s)	$\mathbf{0.36} \times 10^{-3}$	$\mathbf{0.35} \times 10^{-3}$	$\mathbf{0.36} \times 10^{-3}$	$\mathbf{0.35} \times 10^{-3}$

the component of the lunar UERE metric, which will be discussed in the next two subsections.

For a given Microchip CSAC (17 cm^3·0.0035 kg·0.12 W), whose low SWaP characteristics are given in Table 2, Figure 5 provides an illustration of the variation in timing errors across the four orbit types, namely, ELFO, NRHO, LLO, and PCO. In Figure 5, the same color coding is used as that in Figures 2 and 3 to denote different orbit types, with ELFO indicated in orange, NRHO in green, LLO in magenta, and PCO in blue. As stated above in the description of validation metrics, the measurement update rate is reduced by setting the sampling period to $T_{\text{meas}} = mT_{\text{pred}}$, where $m = 5$.

Three orbit types, namely, ELFO, NRHO, and PCO, demonstrate comparable RMS timing errors of $< 4.08 \times 10^{-2}$ μs in clock bias and $< 4.07 \times 10^{-2}$ ns/s in clock drift, while the case study based on the LLO shows a higher RMS error in clock bias of $< 6.79 \times 10^{-2}$ μs. This observation implies that the lowest RMS timing error not only depends on the shortest maximum ECOP and the greatest satellite visibility but also on orbital parameters, namely, the eccentricity, inclination, and altitude, which govern the geometric configuration between the Earth GPS and LNSS. Note that there is only a small degree of correlation between the orbital viewing geometry for the least stable clock, i.e., CSAC. This trend occurs because the mean distance between the Earth GPS and the lunar navigation satellite is already quite large (approximately 385000 km); thus, altitude variations in the lunar orbit, which are on the order of only thousands, are not sufficient to induce a significant

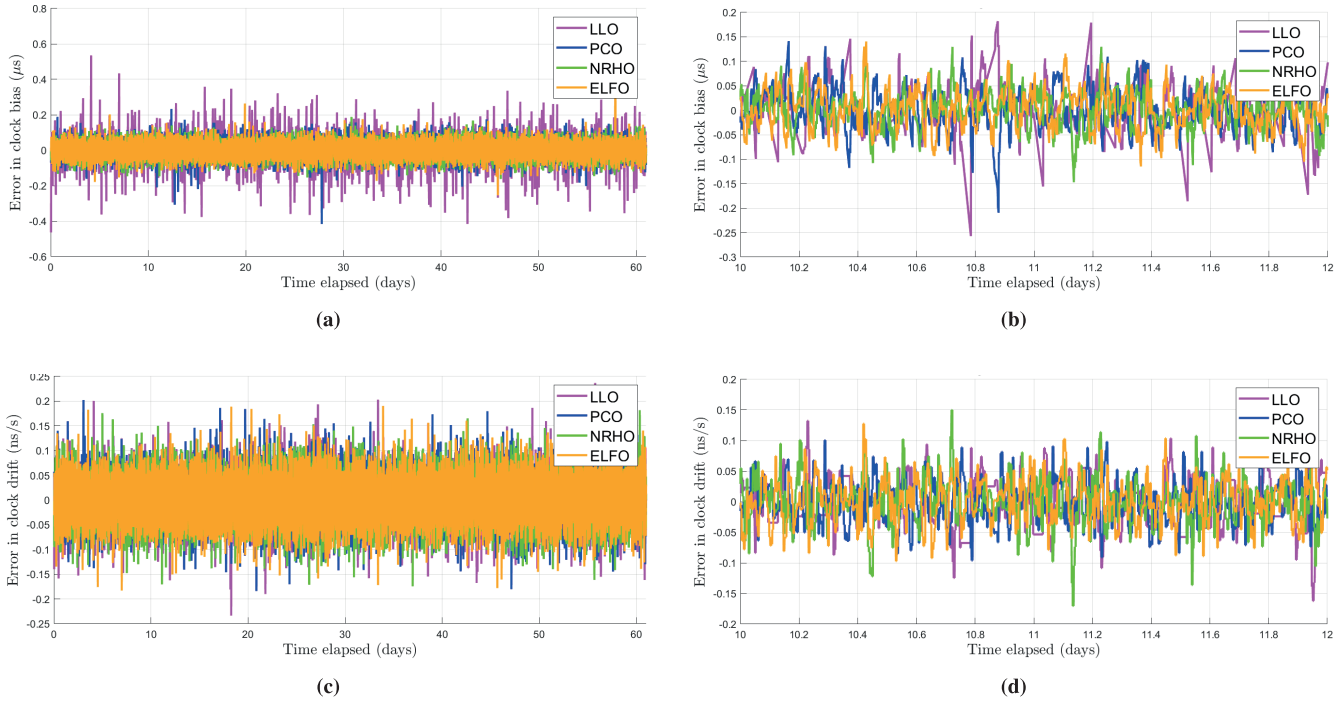

FIGURE 5 Comparison of estimation errors in clock bias and drift across different orbit types with an onboard Microchip CSAC
ELFO is indicated in orange, NRHO in green, LLO in magenta, and PCO in blue. (a) and (c) demonstrate the errors in clock bias and clock drift for the entire experiment duration, respectively, while (b) and (d) present magnified errors in clock bias and clock drift for a smaller time segment of 2 days. Three of the orbit types, namely, the ELFO, NRHO, and PCO, demonstrate comparable RMS timing errors of < 0.0408 μs in clock bias and < 0.0407 ns/s in clock drift, while the LLO exhibits a slightly higher RMS error in clock bias of 0.0679 μs.

difference in timing error. This observation is interesting, as it ensures uniformity in the accuracy of onboard clock estimates, even if a hybrid constellation involving varied lunar orbit types is considered in the future LNSS.

Additionally, a larger RMS timing error for any case study can indicate a larger timing error in either of the two segments: a) when at least one Earth-GPS satellite is visible and b) at the end of the ECOP (during the ECOP, only a prediction update is executed; thus, the estimation errors continue to increase). For instance, the largest RMS error in clock bias (6.79×10^{-2} μs) for the LLO–CSAC among all case studies can be attributed to the following factors: a) the least stable clock (i.e., CSAC) among different clock types combined with a significant ECOP of 2880 s and b) a poor visibility for at least one Earth-GPS satellite of only 61.5% (as shown in Table 3). These factors cause the estimation errors both during and at the end of the ECOPs to be higher (as depicted by magenta spikes in Figure 5[a]). Note that while the LLO trades unfavorably in terms of orbit stability, ECOP, and satellite visibility, its key advantage lies in its low orbiting altitude. From a SmallSats perspective, the smaller distance of the LLO from the lunar surface users enables the use of smaller antennas for transmitting lunar navigation signals. As shown in Table 4, as the SWaP and timing stability of the onboard clock increase, the variation in RMS error across orbit types becomes less significant, wherein the RMS error in clock bias and drift for DSAC are $< 0.87 \times 10^{-2}$ μs and $< 0.46 \times 10^{-3}$ ns/s, respectively. The RMS value for DSAC is significantly lower (approximately one order of magnitude) than those of the other clock types, namely, CSAC, MAC, PRS10, and RAFS. This result occurs because the TDEV per day and PSD coefficients of the DSAC,

as presented in Table 2, are also significantly lower than those of the other clock types, indicating a higher timing stability for NASA's DSAC. A lower RMS timing error for DSAC also indicates smaller errors at the end of the ECOPs compared with other clock types.

4.4 | Across Case Studies and Earth-GPS Measurement Update Rates: Sensitivity Analysis of the Lunar UERE

The motivation behind the sensitivity analysis is to quantify the variation in the lunar UERE as the Earth-GPS measurement update rate is varied. Note that quantifying the power saved by the use of less frequent Earth-GPS measurements requires a more complex analysis, which is beyond the scope of this paper. Figure 6(a) demonstrates the variation in lunar UERE metric across the case studies examined in this work while considering no reduction in the measurement update rate, i.e., setting $T_{\text{meas}} = T_{\text{pred}} = 60$ s or $m = 1$. The proposed time transfer achieves a low lunar UERE of < 10 m for most case studies, except for the case study involving the LLO and the Microchip CSAC, which exhibits a value of 18.4 m. These observations imply that if the desired lunar UERE to be maintained by an LNSS satellite is, for instance, < 10 m at all times, one can easily opt for an onboard clock

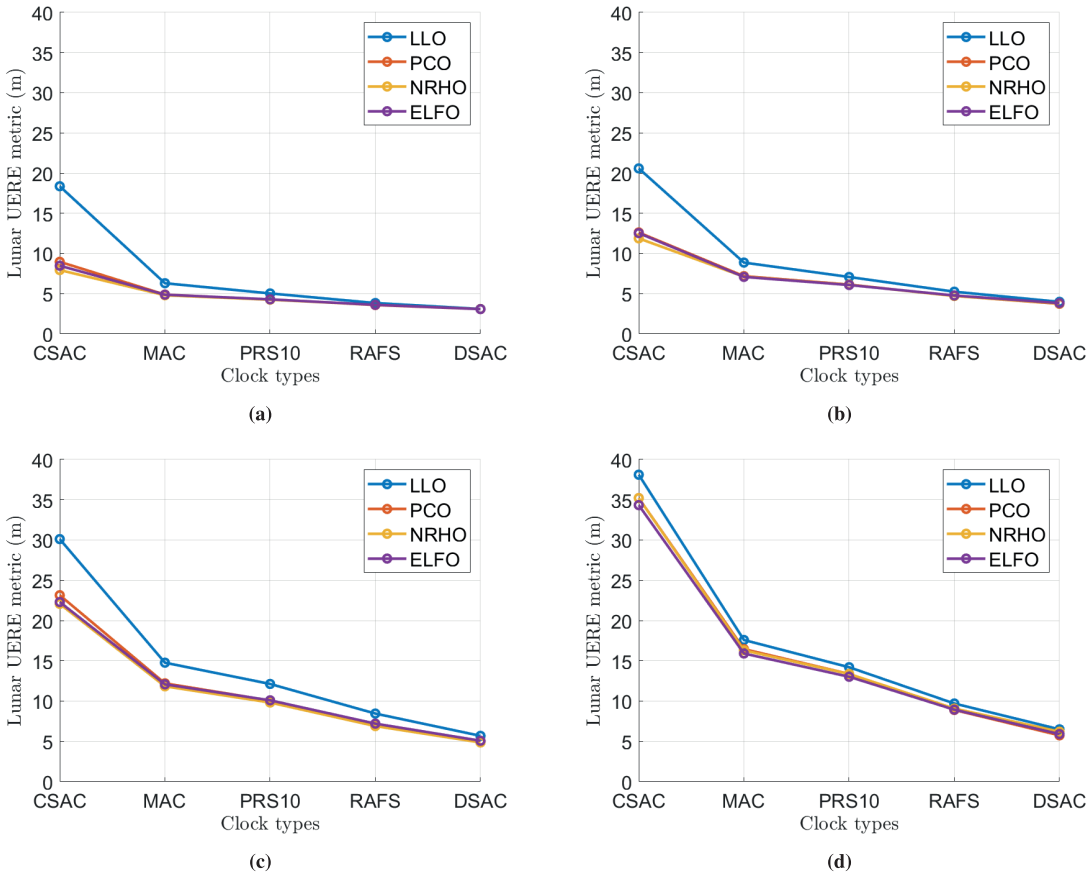

FIGURE 6 Sensitivity analysis of the lunar UERE metric across different case studies for reduced measurement update rates
(a) $m = 1$ is the baseline case with no reduction in the measurement update rate, i.e., $T_{\text{meas}} = T_{\text{pred}}$, (b) $m = 5$, (c) $m = 30$, and (d) $m = 60$.

that falls in the lower end of the SWaP spectrum, such as the Microchip CSAC (17 cm^3·0.0035 kg·0.12 W) or Microchip MAC (50 cm^3·0.0084 kg·0.5 W), instead of a high-SWaP clock, such as Excelitas' RAFS or NASA's DSAC. To maintain a desired lunar UERE, one can also wisely choose an orbit type that is easy to maintain and has a longer lifespan, such as the LLO, PCO, or ELFO, over the more complex NRHO, which requires constant station-keeping maneuvers to maintain stability. Furthermore, for future investigations, the future SmallSat-based lunar PNT constellation could potentially be heterogeneous, wherein the grade of the onboard clock is chosen based on the orbit of each LNSS satellite to satisfy a desired lunar UERE. For instance, to maintain a desired lunar UERE of < 5 m, Figure 6(a) demonstrates the potential of designing a heterogeneous LNSS constellation based on an ELFO or LLO, wherein the satellites in an LLO can be equipped with a PRS10 clock while the satellites in an ELFO can be equipped with a lower-SWaP Microchip MAC.

Figures 6(b)–6(d) show the variation in lunar UERE metric for three cases of reduced update rates, where $T_{meas} = mT_{pred}$ with $m = 5$, $m = 30$, and $m = 60$ respectively. As the Earth-GPS measurement update rate increases for low-SWaP clocks with sampling periods from $T_{meas} = 60$ min $(m = 60)$ to $T_{meas} = 1$ min $(m = 1)$, an increased sensitivity of the lunar UERE metric is observed across lunar orbit types, i.e., the difference in value between the LLO and other orbit types increases. Additionally, the estimated lunar UERE is < 30 m for a reduced Earth-GPS measurement update rate with a sampling period of up to $T_{meas} = 30$ min, which is comparable in order of magnitude to that of the baseline case with $m = 1$ (in Figure 6[a]) as well as the legacy Earth GPS. Thus, even at a reduced measurement update rate, the LNSS design, which utilizes time transfer from the Earth GPS, lowers the SWaP requirements of the onboard clock. Furthermore, one can re-observe the potential for a heterogeneous, SmallSat-based PNT constellation explained above, wherein not only the grade of the onboard clock is carefully chosen, but also the reduced update rate of the timing filter based on the LNSS satellite orbit so as to satisfy a desired lunar UERE.

5 | CONCLUSION

We performed an exhaustive case study analysis for designing a SmallSat-based LNSS with time transfer from the Earth GPS, wherein trade-offs between different design considerations related to the onboard clock and lunar orbit type were investigated. In the proposed time-transfer approach, the SWaP requirements of the onboard clocks were alleviated by leveraging the intermittently available Earth-GPS signals to provide timing corrections. The lunar UERE metric was also designed to characterize the ranging accuracy of LNSS satellites.

Using high-fidelity simulations of an LNSS satellite in the STK software of Analytical Graphics, Inc., multiple case studies were designed comprising five onboard clocks and four lunar orbit types. The shortest maximum ECOP of only 420 s was observed for an NRHO because this orbit type experiences fewer occultations from Earth and the Moon given its high altitude. A low lunar UERE of < 30 m was demonstrated for low-SWaP onboard clocks (e.g., Microchip CSAC, SRS PRS10) even for reduced Earth-GPS measurement update rates with sampling periods of up to 30 min. Through a case study analysis of time transfer from the Earth GPS, lower-SWaP onboard clocks and easier-to-maintain lunar orbit types were shown to still achieve the desired lunar UERE across the entire LNSS constellation. In this context, the easier-to-maintain lunar orbit types are those with

higher orbital stability and longer lifespans, such as the LLO, PCO, or ELFO, in contrast to the more complex NRHO, which requires constant station-keeping maneuvers. Similarly, the lower-SWAP onboard clocks are those that fall in the lower end of the SWaP spectrum, such as the Microchip CSAC or Microchip MAC, instead of a high-SWaP clock, such as Excelitas's RAFS or NASA's DSAC. Based on this single-satellite analysis of the time-transfer architecture, future work will include the design of a SmallSat-based LNSS constellation that provides reliable and precise PNT services to support upcoming lunar exploration missions. Preliminary work based on this concept has been recently published in Bhamidipati, Mina, Sanchez, et al., 2022.

ACKNOWLEDGMENTS

We thank the Analytical Graphics, Inc. educational alliance program for providing us with the STK software license to perform this research. We also thank Keidai Ilyama for insightful discussions related to this work and Daniel Neamati for reviewing this paper.

REFERENCES

AGI. (2021). Systems Tool Kit (STK). *AGI*. https://www.agi.com/products/stk

Almat, N. (2020). *Metrological and stability studies in high-performance rubidium vapor-cell atomic clocks* (Doctoral dissertation). University of Neuchatel. https://doi.org/10.35662/unine-thesis-2836

Baird, D. (2019). Record-breaking satellite advances NASA's exploration of high-altitude GPS. *NASA*. https://www.nasa.gov/feature/goddard/2019/record-breaking-satellite-advances-nasa-s-exploration-of-high-altitude-gps

Bhamidipati, S., Mina, T., & Gao, G. (2021). Design considerations of a lunar navigation satellite system with time-transfer from Earth-GPS. *Proc. of the 34th International Technical Meeting of the Satellite Division of the Institute of Navigation (ION GNSS+ 2021)*, St. Louis, MO, 950–965. https://doi.org/10.33012/2021.18021

Bhamidipati, S., Mina, T., & Gao, G. (2022a). Time transfer from GPS for designing a SmallSat-based lunar navigation satellite system. *NAVIGATION, 69*(3). https://doi.org/10.33012/navi.535

Bhamidipati, S., Mina, T., & Gao, G. (2022b). A case study analysis for designing a lunar navigation satellite system with time-transfer from Earth-GPS. *Proc. of the 2022 International Technical Meeting of the Institute of Navigation*, Long Beach, CA. 407–419. https://doi.org/10.33012/2022.18202

Bhamidipati, S., Mina, T., Sanchez, A., & Gao, G. (2022). A lunar navigation and communication satellite system with Earth-GPS time transfer: Design and performance considerations. *Proc. of the 35th International Technical Meeting of the Satellite Division of the Institute of Navigation (ION GNSS+2022)*, Denver, CO, 537–553. https://doi.org/10.33012/2022.18365

Borio, D., Sokolova, N., & Lachapelle, G. (2011). Doppler measurement accuracy in standard and high-sensitivity global navigation satellite system receivers. *IET Radar, Sonar & Navigation*, *5*(6), 657–665. https://doi.org/10.1049/iet-rsn.2010.0249

Capuano, V., Basile, F., Botteron, C., & Farine, P. A. (2015). GNSS-based orbital filter for Earth Moon transfer orbits. *Journal of Navigation*, *69*(4), 745–764. https://doi.org/10.1017/s0373463315000843

Capuano, V., Botteron, C., Leclère, J., Tian, J.,Wang, Y., & Farine, P. A. (2015). Feasibility study of GNSS as navigation system to reach the Moon. *Acta Astronautica*, *116*, 186–201. https://doi.org/10.1016/j.actaastro.2015.06.007

Cheung, K.-M., Lee, C., & Heckman, D. (2020). Feasibility of "weak GPS" real-time positioning and timing at lunar distance. *2020 IEEE Aerospace Conference*, Big Sky, MT. 1–7. https://doi.org/10.1109/aero47225.2020.9172327

Cozzens, T. (2021). Galileo will help Lunar Pathfinder navigate around Moon. *GPS World*. https://www.gpsworld.com/galileo-will-help-lunar-pathfinder-navigate-around-moon/

Delépaut, A., Schönfeldt, M., Giordano, P., Blonski, D., Sarnadas, R., Ries, L., & Ventura-Traveset, J. (2019). A system study for cislunar radio navigation leveraging the use of realistic galileo and GPS signals. *Proc. of the 32nd International Technical Meeting of the Satellite Division of the Institute of Navigation (ION GNSS+ 2019)*, Miami, FL. 1199–1219. https://doi.org/10.33012/2019.17084

Delépaut, A., Giordano, P., Ventura-Traveset, J., Blonski, D., Schönfeldt, M., Schoonejans, P., Aziz, S., & Walker, R. (2020). Use of GNSS for lunar missions and plans for lunar in-orbit development. *Advances in Space Research*, *66*(12), 2739–2756. https://doi.org/10.1016/j.asr.2020.05.018

Donaldson, J. E., Parker, J. J., Moreau, M. C., Highsmith, D. E., & Martzen, P. D. (2020). Characterization of on-orbit GPS transmit antenna patterns for space users. *NAVIGATION, 67*(2), 411–438. https://doi.org/10.1002/navi.361

Ely, T., Prestage, J., Tjoelker, R., Burt, E., Dorsey, A., Enzer, D., Herrera, R., Kuang, D., Murphy, D., Robison, D., Seal, G., Stuart, J., Wang, R., & Seubert, J. (2022). Deep space atomic clock technology demonstration mission results. *Proc. of the 2022 IEEE Aerospace Conference (AERO)*, Big Sky, MT. 1–20. https://doi.org/10.1109/aero53065.2022.9843303

Ely, T. A., Burt, E. A., Prestage, J. D., Seubert, J. M., & Tjoelker, R. L. (2018). Using the deep space atomic clock for navigation and science. *IEEE Transactions on Ultrasonics, Ferroelectrics, and Frequency Control*, *65*(6), 950–961. https://doi.org/10.1109/tuffc.2018.2808269

Ely, T. A., & Lieb, E. (2006). Constellations of elliptical inclined lunar orbits providing polar and global coverage. *The Journal of the Astronautical Sciences*, *54*(1), 53–67. https://doi.org/10.1007/bf03256476

Folta, D., & Quinn, D. (2006). Lunar frozen orbits. *AIAA/AAS Astrodynamics Specialist Conference and Exhibit*. https://doi.org/10.2514/6.2006-6749

InsideGNSS. (2021). ESA, NASA race to the Moon for first lunar GNSS fix. *Inside GNSS*. https://insidegnss.com/esa-nasa-race-to-the-moon-for-first-lunar-gnss-fix/

Israel, D. J., Mauldin, K. D., Roberts, C. J., Mitchell, J. W., Pulkkinen, A. A., Cooper, L. V. D., Johnson, M. A., Christe, S. D., & Gramling, C. J. (2020). LunaNet: A flexible and extensible lunar exploration communications and navigation infrastructure. *2020 IEEE Aerospace Conference*, Big Sky, MT. 1–14. https://doi.org/10.1109/aero47225.2020.9172509

Johnson-Groh, M. (2016). NASA's MMS breaks Guinness world record. *NASA*. https://www.nasa.gov/feature/goddard/2016/nasa-s-mms-breaks-guinness-world-record

Kaplan, E. D., & Hegarty, C. (2017). *Understanding GPS/GNSS: Principles and applications*. Artech House. https://dl.acm.org/doi/10.5555/3158927

Kraft, R. (2020). NASA enlists commercial partners to fly payloads to Moon. *NASA*. https://www.nasa.gov/feature/nasa-enlists-commercial-partners-to-fly-payloads-to-moon

Krawinkel, T., & Schön, S. (2015). Benefits of receiver clock modeling in code-based GNSS navigation. *GPS Solutions*, *20*(4), 687–701. https://doi.org/10.1007/s10291-015-0480-2

Laurini, K. C., & Gerstenmaier, W. H. (2014). The global exploration roadmap and its significance for NASA. *Space Policy*, *30*(3), 149–155. https://doi.org/10.1016/j.spacepol.2014.08.004

Lutwak, R. (2011). The SA. 45s chip-scale atomic clock–early production statistics. *Proc. of the 43rd Annual Precise Time and Time Interval Systems and Applications Meeting (PTTI 2011)*, Long Beach, CA. 207–220. https://www.ion.org/publications/abstract.cfm?articleID=10786

Mabrouk, E. (2015). What are smallsats and cubesats? *NASA*. https://www.nasa.gov/content/what-are-smallsats-and-cubesats

Melosh, H. J., Freed, A. M., Johnson, B. C., Blair, D. M., Andrews-Hanna, J. C., Neumann, G. A., Phillips, R. J., Smith, D. E., Solomon, S. C., Wieczorek, M. A., & Zuber, M. T. (2013). The origin of lunar mascon basins. *Science*, *340*(6140), 1552–1555. https://doi.org/10.1126/science.1235768

Montenbruck, O., Gill, E., & Lutze, F. (2002). Satellite orbits: Models, methods, and applications. *Applied Mechanics Reviews*, *55*(2), B27. https://doi.org/10.1115/1.1451162

National Aeronautics and Space Administration. (2022). Lunar communications relay and navigation systems (LCRNS). *Preliminary Lunar Relay Services Requirements Document (SRD)*. https://esc.gsfc.nasa.gov/static-files/ESC-LCRNS-REQ-0090%20RevA%2011-04-2022.pdf

Parker, J. J., Dovis, F., Anderson, B., Ansalone, L., Ashman, B., Bauer, F. H., D'Amore, G., Facchinetti, C., Fantinato, S., Impresario, G., McKim, S. A., Miotti, E., Miller, J. J., Musmeci, M., Pozzobon, O., Schlenker, L., Tuozzi, A., & Valencia, L. (2022). The lunar GNSS receiver experiment (LuGRE). *Proc. of the 2022 International Technical Meeting of the Institute of Navigation*, Long Beach, CA. 420–437. https://doi.org/10.33012/2022.18199

Schmittberger, B. L., & Scherer, D. R. (2020). A review of contemporary atomic frequency standards. *arXiv preprint, arXiv:2004.09987*. https://arxiv.org/pdf/2004.09987.pdf

Schonfeldt, M., Grenier, A., Delépaut, A., Giordano, P., Swinden, R., Ventura-Traveset, J., Blonski, D., & Hahn, J. (2020). A system study about a lunar navigation satellite transmitter system. *Proc. of the 2020 European Navigation Conference (ENC)*, Dresden, Germany. 1–10. https://doi.org/10.23919/enc48637.2020.9317521

Schönfeldt, M., Grenier, A., Delépaut, A., Giordano, P., Swinden, R., & Ventura-Traveset, J. (2020). Across the lunar landscape: Towards a dedicated lunar PNT system. *Inside GNSS*. https://insidegnss.com/across-the-lunar-landscape-towards-a-dedicated-lunar-pnt-system/

Seubert, J., Ely, T. A., & Stuart, J. (2022). Results of the deep space atomic clock deep space navigation analog experiment. *Journal of Spacecraft and Rockets*, 1–12. https://doi.org/10.2514/1.a35334

Smith, M., Craig, D., Herrmann, N., Mahoney, E., Krezel, J., McIntyre, N., & Goodliff, K. (2020). The Artemis program: An overview of NASA's activities to return humans to the Moon. *2020 IEEE Aerospace Conference*, Big Sky, MT. 1–10. https://doi.org/10.1109/aero47225.2020.9172323

Van Dierendonck, A. J., & McGraw, J. (1984). Relationship between Allan variances and Kalman filter parameters. *Proc. of the 16th Annual Precise Time and Time Interval Systems*

and Applications Meeting, Greenbelt, Maryland. 273–293. https://www.ion.org/publications/abstract.cfm?articleID=16168

Wertz, J. R., Everett, D. F., & Puschell, J. J. (2011). *Space mission engineering: The new SMAD*. Microcosm Press.

Whitley, R., & Martinez, R. (2016). Options for staging orbits in cislunar space. *Proc. of the 2016 IEEE Aerospace Conference*, Big Sky, MT. https://doi.org/10.1109/aero.2016.7500635

Williams, J., Lee, D. E., Whitley, R. J., Bokelmann, K. A., Davis, D. C., & Berry, C. F. (2017). Targeting cislunar near rectilinear halo orbits for human space exploration. *Proc. of the 27th AAS/AIAA Space Flight Mechanics Meeting*, San Antonio, TX. (JSC-CN-38615). https://www.researchgate.net/publication/322526659_Targeting_Cislunar_Near_Rectilinear_Halo_Orbits_for_Human_Space_Exploration

Winternitz, L., Moreau, M., Sirotzky, S., et al. (2004). Navigator GPS receiver for fast acquisition and weak signal space applications. *Proc. of the 17th International Technical Meeting of the Satellite Division of the Institute of Navigation (ION GNSS 2004)*, Long Beach, CA. 1013–1026. https://www.ion.org/publications/abstract.cfm?articleID=5777

Winternitz, L. B., Bamford, W. A., Long, A. C., & Hassouneh, M. (2019). GPS based autonomous navigation study for the lunar gateway. *Annual American Astronautical Society (AAS) Guidance, Navigation, and Control Conference*, (AAS 19-096), Breckenridge, CO. https://ntrs.nasa.gov/citations/20190002311

Winternitz, L. B., Bamford, W. A., Price, S. R., Carpenter, J. R., Long, A. C., & Farahmand, M. (2017). Global positioning system navigation above 76,000 km for NASA's magnetospheric multiscale mission. *NAVIGATION*, *64*(2), 289–300. https://doi.org/10.1002/navi.198

Zucca, C., & Tavella, P. (2005). The clock model and its relationship with the allan and related variances. *IEEE Transactions on Ultrasonics, Ferroelectrics and Frequency Control*, *52*(2), 289–296. https://doi.org/10.1109/tuffc.2005.1406554

How to cite this article: Bhamidipati, S., Mina, T., & Gao, G. (2023). A case study analysis for designing a lunar navigation satellite system with time transfer from the earth GPS. *NAVIGATION, 70*(4). https://doi.org/10.33012/navi.599